formance is still to be measured when good weather conditions will allow us to observe a star in the sky of Neusäß.

With an optical design optimised for the targets of the technical commissioning of the VLTI and its instruments, with high-quality optics, high rigidity of the mechanics and good control electronics, the two siderostats to be installed early 2000 will offer the capability to characterise the VLTI in its first phase. As done for the Astronomical Seeing Monitor, it is envisaged to upgrade the CCD camera by a VLT technical CCD and to perform the necessary upgrade of the control electronics and software to fully meet the ESO VLT standard.

Table 1: List of sources bright enough to be used with 400-mm diameter siderostats (C means N magnitude corresponding to correlated flux).

#	Object	1950 Coordinates	Magnitudes	
1	Alfa Ori	52 27.8 +07 23 58:	V=0.5	C=–4.5
2	Alfa Sco	26 17.9 –26 19 19:	V=1.0	C=–4.0
3	Alfa Tau	33 03.0 +16 24 30:	V=1.5	C=–3.0
4	L2 Pup	12 01.8 –44 33 17:	V=5.1	C=–3.0
5	R Leo	44 52.1 +11 39 41:	V=6.0	C=–3.0
6	IRC + 10 216	45 14.2 +13 30 40:		C=–3.0
7	V766 Cen	43 40.3 –62 20 25:	V=6.5	C=–3.0
8	Alfa Her	12 21.6 +14 26 46:	V=3.5	C=–3.0
9	VX Sgr	05 02.5 –22 13 56:		C=–3.2
10	R Aqr	41 14.1 –15 33 46:	V=6.4	C=–3.1

Myopic Deconvolution of Adaptive Optics Images

J.C. CHRISTOU[1], D. BONACCINI[2], N. AGEORGES[2], and F. MARCHIS[3]

[1]US Air Force Research Laboratory, Kirtland AFB, New Mexico, USA (christou@as.arizona.edu)
[2]ESO, Garching bei München, Germany (dbonacci@eso.org, nageorge@eso.org)
[3]ESO, Santiago, Chile (fmarchis@eso.org)

Abstract

Adaptive Optics produces diffraction-limited images, always leaving a residual uncorrected image and sometime PSF artifacts due, e.g., to the deformable mirror. Post-processing is in some cases necessary to complete the correction and fully restore the image. The results of applying a multi-frame iterative deconvolution algorithm to simulated and actual Adaptive Optics data are presented, showing examples of the application and demonstrating the usefulness of the technique in Adaptive Optics image post-processing. The advantage of the algorithm is that the frame-to-frame variability of the PSF is beneficial to its convergence, and the partial knowledge of the calibrated PSF during the observations is fully exploited for the convergence. The analysis considers the aspects of morphology, astrometry, photometry and the effect of noise in the images. Point sources and extended objects are considered.

1. Introduction

This paper reports on work done to establish and evaluate data reduction procedures specifically applicable to Adaptive Optics (AO) data. The programme evaluated for multi-frame iterative blind deconvolution, IDAC, is provided by J. Christou and available in the ESO Web page at `http://www.ls.eso.org/lasilla/Telescope/360cat/adonis/html/datared.html#distrib` for the Unix platforms.

This work is part of a dedicated effort to guide the AO users in the data reduction process and to produce specific data-reduction tools. The observing data presented here were taken with Adonis at the La Silla 3.6-m telescope during technical time, specifically dedicated to this data-reduction programme.

Adaptive Optics (AO) is now a proven technology for real-time compensation of space objects, to remove the degrading effects of the Earth's atmosphere. However, the compensation is never "perfect" and residual wavefront errors remain, which in some cases can lead to significant uncompensated power. This decreases the image contrast making, in some cases, necessary to use some form of image post-processing to remove the effects of the system's point spread function (PSF). The knowledge of good deconvolution techniques suitable on AO images is also important to boost images with low Strehl, e.g. from low-order AO systems.

AO compensation is achieved via a servo-control loop which uses a reference signal from a guide star (GS) to zero the wavefront error at each iteration, typically every 2–40 msec chosen depending on the observing wavelength and reference signal strength. It is well known that the performance of an AO system is limited by the reference signal strength as well as by the atmospheric coherence length r_0, the atmospheric coherence time to, and the isoplanatic angle θ_0.

In astronomical imaging, exposure times from a few msec to tens of minutes are used. The variability of r_0 and of the AO PSF can be quite large in short integration times (seconds), while it smoothes out in timescales of minutes. There is also a slow decline in Strehl Ratio (SR), the system's performance parameter[1], across an imaging field of radius θ_0 due to field anisoplanatism effect. The latter produces mainly an elongation of the PSF in the direction of the GS, which is function of the object radial distance. The PSF at the reference star has a diffraction-limited core, surrounded by a broad gaussian halo.

Static and dynamic artifacts in the image due to either print-through of the deformable mirror actuators, and differential aberrations between the science and WFS optical paths, have also been observed. For ADONIS, the former have a Gaussian shape with peak intensities in the range of 0.5% to 1% of the central PSF core. Although their energy content is undoubtedly small, if not removed they make it difficult to unambiguously identify faint objects or faint structures around bright sources.

Thus the observer has to worry about time-varying and space-varying AO PSFs.

In general, the observation of a point source as PSF Calibrator, in addition to the target, is used to further improve the compensated image via post-processing. However, the AO compensation obtained on the target and the PSF calibrator are not necessarily the same: the

---

[1] The Strehl Ratio is a standard measure for the performance of an AO system. It is the ratio of the maximum intensity of the delivered PSF to the maximum of the theoretical diffraction-limited PSF when both PSFs are normalised to unity. A Strehl Ratio of 1 means achievement of the theoretically best performance.

AO compensation depends upon the atmospheric statistics, i.e. the coherence length r_0 and the correlation time t_0, and how they relate to the sub-aperture size and sampling time of the AO system. These parameters vary in time between sets of observations of the target and the PSF calibrator, so that the AO system performs differently on each. In addition, the AO system is sensitive to the brightness and extent of the source used to close the loop. Both affect the signal-to-noise (SNR) on the wavefront sensor (WFS). In other words, the PSF calibrator obtained 'off-line' from the science observation does not give exactly the same PSF of the science frames, and the PSF is only approximately known.

So far, WFS using Avalanche Photodiodes (APD) in photon-counting mode have been used to rebuild the PSF from WFS data (J.P. Véran et al., 1997), obtained during the science acquisition. The method proves rather precise as long as the guide star is a point object and not too faint. Still, only an approximate PSF is recovered, especially with faint GS or with short exposure times.

Thus, in order to deconvolve the AO observations, it is useful to use an algorithm that is flexible with regard to the PSF as the latter is always known only with limited precision. A "blind" deconvolution algorithm is very suitable for this application. We call it 'myopic' as the AO PSF is rather well known, although not perfectly, either via the PSF calibrator method or via the PSF reconstruction from WFS data.

We report here on the iterative 'myopic' deconvolution technique, which takes advantage of multiple frames taken under variable PSF conditions. Starting from an approximately known average PSF, and assuming that the science object is constant in time, the algorithm runs relaxing the PSF in each frame and finding the best combination of PSFs which deliver the common science object in all the frames. The input is an approximated average PSF and a set of N science frames taken with the same instrumental set-up. The output is the science object recovered, and a set of N PSFs. In general, the more the PSF varies between frames, the easier the science object detection is. As it is known that the PSF in closed loop varies in time scales of seconds, this myopic iterative deconvolution algorithm is very well suited to AO data. Long-exposure images taken in different seeing conditions, e.g. with different PSFs, also benefit from this deconvolution method.

Deconvolution algorithms use a "known" PSF to deconvolve the measurement. This is classically an ill-posed inverse problem which has been well studied in recent years, and algorithms such as Lucy-Richardson are readily available (Lucy, 1974). Multiframe iterative blind deconvolution (IBD), which solves for both the object and PSF simultaneously, is ill-posed as well and also poorly determined. However, the application of physical constraints upon this algorithm permits both the object and PSF to be recovered to an accuracy that depends mainly upon the SNR of the observations (Sheppard et al., 1998).

We discuss the physically constrained iterative deconvolution algorithm, described in section 2, and its application to both simulated and real data sets described in sections 3 and 4. The simulations permit us to investigate the algorithm's performance given a known target. We briefly show the effect of noise on photometry, astrometry and morphology. Different data types are investigated including multiple point source targets, binary stars, a galaxy image, Io and RAqr for different SNR conditions. This permits performance evaluations on real data sets by comparison to the predictions of the simulations. As previously mentioned, the algorithm also recovers the PSFs for the observations, and investigation of these permit evaluation of the AO system's performance e.g. on non-point-like targets.

We are assuming that the PSF is constant across the processed field of view, i.e. we neglect anisoplanatism effects. Work on the latter is in progress at ESO in collaboration with the Osservatorio Astronomico di Bologna, and it will be reported later.

2. The Algorithm

The IDAC code is based on the conjugate gradient error-metric minimisation, blind deconvolution algorithm of Jefferies and Christou (1993) and is currently under further development and testing by an extended group. The advantage of multiple frames is to have more information to break the symmetry of the problem. For a single frame, the target and PSF are exchangeable without using prior information. For multiple frames, a common object solution is computed along with the corresponding PSF for each observation in the data set. Note that PSF static artifacts in the image will be considered part of the object, and have to be calibrated out. This is done in several ways, e.g. processing the PSF calibrator data with this same code, extracting the static components and removing them from the science object at the end of the processing, or using images of an artificial point source on the AO setup.

The standard isoplanatic imaging equation can be written as

$$g'(\vec{r}) = f(\vec{r}) * h(\vec{r}) + n(\vec{r}) \quad (1)$$

or in the Fourier domain as

$$G'(\vec{f}) = F(\vec{f}) \cdot H(\vec{f}) + N(\vec{f}) \quad (2)$$

where $g'(\vec{r})$ is the measurement, $f(\vec{r})$ is the target, $h(\vec{r})$ is the blur or PSF of the system and * denotes convolution. $n(\vec{r})$ represents noise contamination which can be some combination of photon noise and detector noise. The Fourier transforms are indicated by the corresponding uppercase notation, where $\vec{r}$ is the spatial index and $\vec{f}$ is the spatial frequency index.

For the blind deconvolution case, both the target and PSF are unknown quantities. In order to solve for these we apply an error-metric minimisation scheme using a conjugate gradient algorithm simultaneously minimising on several error-metric terms. The first is known as the fidelity term which measures the consistency between the measurements and the estimates.

$$E_{\mathrm{F}} = \sum_{k} \sum_{i \in R} | g'_{ik} - \hat{f}_i * \hat{h}_{ik} | \cdot s_{ik} \quad (3)$$

where k is the frame index and i is the pixel index and s_{ik} is a "bad" pixel mask which eliminates cosmic-ray events and "hot" and "dead" pixels from the summation. The ^ indicates the current estimates of the variables.

One of the problems with many of these iterative algorithms is knowing when to terminate the iterations. From (1) and (3) it can be seen that when an exact solution is reached, the error-metric does not go to zero but to a noise bias, i.e.

$$\begin{aligned} E_{\mathrm{F}} &= \sum_{k} \sum_{i} | g'_{ik} - \hat{g}_{ik} | \cdot s_{ik} \\ &= \sum_{k} \sum_{i} | n_{ik} | \cdot s_{ik} = KN\sigma_N^2 \end{aligned} \quad (4)$$

where zero-mean Gaussian noise of rms σ_N has been assumed for K frames and N pixels per frame. Thus, truncating the iterations at this limit is consistent with the noise statistics and is an effective regularisation procedure to minimise "noise amplification error".

It is also necessary to apply physical constraints to both the object and PSF. Both are positive and following the approach of Thiébaut & Conan (1994), we reparameterise both as square quantities, i.e.

$$\hat{f}_i = \phi_i^2 \qquad \text{and} \qquad \hat{g}_{ik} = \varphi_{ik}^2 \quad (5)$$

It is also noted that the PSF is a band-limited function due to the physical nature of the imaging system, i.e. the telescope used has a finite aperture and therefore the PSF has a finite upper-bound to its spatial frequency range $f_c = \Delta/\lambda$. Thus the PSF estimate is penalised for containing information beyond this spatial frequency limit by the following error metric,

$$E_{\mathrm{BL}} = \sum_{k} \sum_{u \in U} H_{uk} \quad \text{for} \quad u > f_c \quad (6)$$

2.1 Myopic deconvolution

Prior PSF information is utilised reducing the PSF parameter space, better avoiding local minima solutions, and also helping to break the symmetry. This is applied in the form of a mean PSF for the multiple-observation data set. In order to remove the effects of mis-registration from one frame to another, the shift-and-add (SAA) or peak-stacked mean of the PSF estimates is computed,

$$(\hat{h}_i)_{\mathrm{SAA}} = \sum_k \hat{h}_{k(i-i_{\mathrm{pk}})} \qquad (7)$$

where i_{pk} is the intensity peak location of the k^{th} frame. The SAA image is then compared to the SAA image of a reference star by using the following error-metric,

$$E_{\mathrm{SAA}} = \sum_k \left[(h_i)_{\mathrm{SAA}} - (\hat{h}_i)_{\mathrm{SAA}}\right]^2 \qquad (8)$$

Equation 3 computes the fidelity term in the image domain. The advantage of this is to permit the application of support constraints to the measurement as well as bad-pixel masks. However, Jefferies & Christou (1993) originally computed EF in the Fourier domain where there is the advantage of applying a bandpass-limit to the observations, i.e. so that those pixels in the Fourier domain which lie outside the cut-off frequency f_c are excluded from the summation. A modification to this is to apply a spatial frequency SNR weighting for those spatial frequencies which lie within the cut-off frequency, i.e.

$$E_{\mathrm{F}} = \sum_k \sum_{u \in U} \left| G'_{uk} - \hat{F}_u \cdot \hat{H}_{uk} \right| \cdot \Theta_{uk} \qquad (9)$$

where Θ_{uk} in the simplistic case is simply a band-pass filter, i.e. is unity for spatial frequencies lower than f_c and zero outside. However, it can also be defined as a low-pass filter customised to the SNR of the data, e.g. an Optimal Filter (in the linear minimum mean squared error sense.)

$$\Theta_{uk} \approx \frac{|G'_{uk}|^2 - |N_{uk}|^2}{|G'_{uk}|^2} \qquad (10)$$

where $|N_{uk}|^2$ is assumed to be white noise and is obtained from the mean value of $|G'_{uk}|^2$ at spatial frequencies > f_c.

The algorithm minimises on the combined error metric of the individual ones described above, i.e.

$$E = E_{\mathrm{F}} + \sum_j \alpha_j E_j \qquad (11)$$

where α_j are weights which regularise each of the additional error-metric terms.

3. Application to Simulated Data

In order to demonstrate the algorithm's performance on AO data, during our study it was first applied to simulations. In this section we present results from application to a simple object – a set of multiple point sources for which the astrometry and photometry can be recovered. The algorithm is next applied to a far more complicated target, a galaxy.

Figure 1 Left: simulated multiple-point source truth (4 sources). Note that each star is centred on a single pixel. Right: sample PSF from the data cube. Note the diffraction-limited core and Airy rings broken up by residual aberrations. (Both images displayed on a square root scale.)

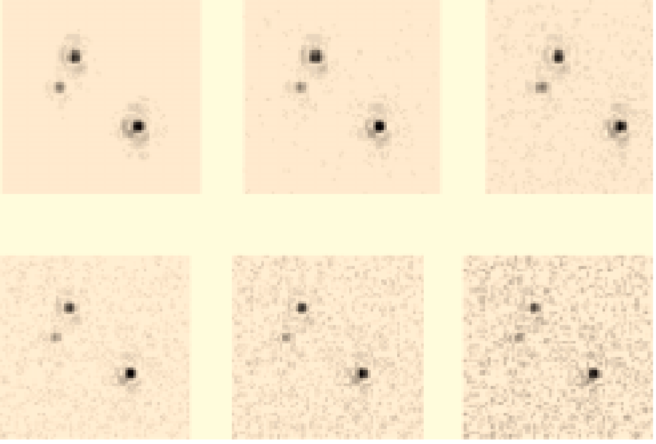

Figure 2: First frame of the data set for the six different SNR cases with the noise increasing from left to right and top to bottom. (All images displayed on a square root scale.)

3.1. Multiple-Star Case

A data set comprised of four point sources was created and convolved with a data cube (64 frames) of simulated atmospheric PSFs for D/r_0 = 2 such that each of the PSFs was dominated by a diffraction-limited core but there was also speckle noise. Figure 1 shows the "truth" object and one of the "truth" PSFs. Six different levels of zero-mean Gaussian noise then contaminated these simulated data. Table 1 gives the SNR levels (or dynamic range) for these cases as defined by the ratio of the peak signal in the data cube to the rms of the noise (PSNR). Figure 2 shows the first frame of the data cube for the six different SNR cases.

For the initial tests, all 64 frames of the data cubes were reduced simultaneously. The algorithm was minimised on the fidelity term (computed in the image domain) and the bandpass constraint only, $E = E_{\mathrm{F}} + E_{\mathrm{BL}}$, using the SAA image of the measurements as the initial object estimate (see Fig. 3) and the SAA image of the brightest source was used as the initial PSF estimate. Note that this source is in fact a close binary. Thus, the algorithm was not run "blind" but reasonable starting "guesses" or estimates were used based on the data. The iterations were terminated when either the noise limit (equation 4) was reached or when the error-metric changed by less than one part in 10^6.

The resulting reconstructed objects are shown in Figure 4. In all six cases. All four sources have been recovered, and in nearly all cases, the individual sources are restored to a single pixel demonstrating the algorithm's ability to "super-resolve". Comparison of the lowest SNR case reconstruction clearly shows detection of the faintest source which is very ambiguous and masked by noise in the raw data (Fig. 2). Comparison to the SAA images (Fig. 3) shows the faintest source to be a "brightening" of the Airy ring around the brightest object. The super-

PSNR (P)	DB [20 $\log_{10}$(P)]	Δ Magnitude
819	58	7.3
410	52	6.5
205	46	5.8
102	40	5.0
51	34	4.2
26	28	3.5

Table 1: Signal-to-noise ratios for the simulated multiple-star data sets given as the ratio of the peak signal to the rms of the additive noise (PSNR) as well as in decibels and stellar magnitudes.

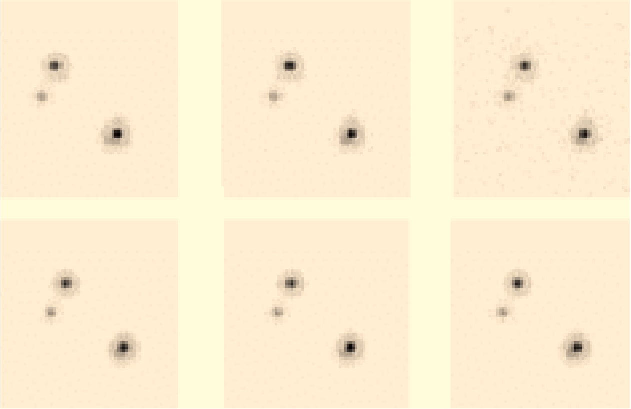

Figure 3: Initial object estimates for the six different SNR cases with the noise increasing from left to right and top to bottom. Note that the brightest source (bottom left) was used as the initial PSF estimate. (All images displayed on a square root scale.)

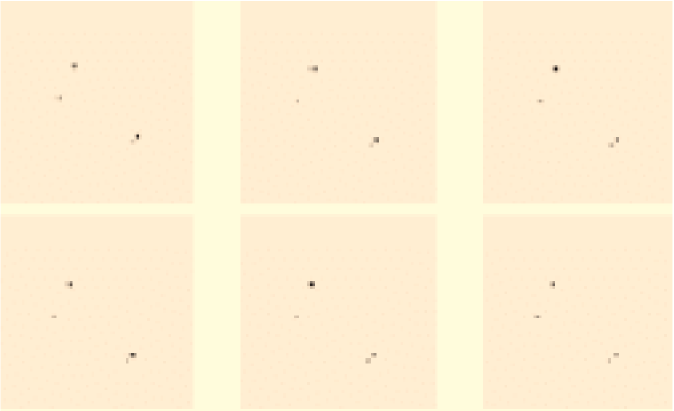

Figure 4: Reconstructed objects for the six different SNR cases with the noise increasing from left to right and top to bottom. (All images displayed on a square root scale.)

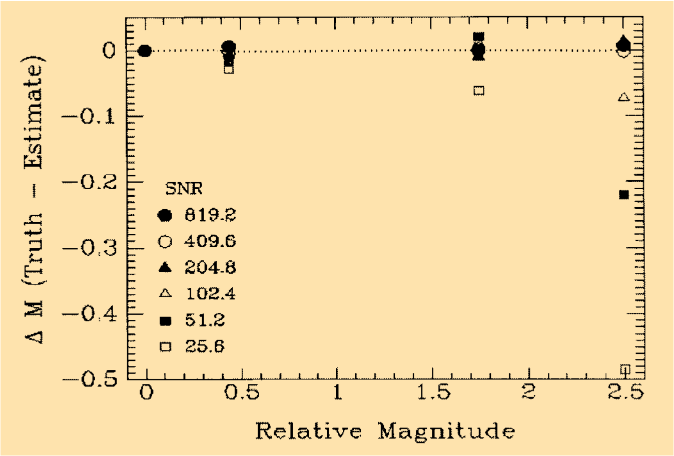

Figure 5: Residual photometry errors from measuring the brightest pixel for the four sources in the object reconstructions for the 6 different SNR cases compared to the sources' true brightness normalised to the brightest source.

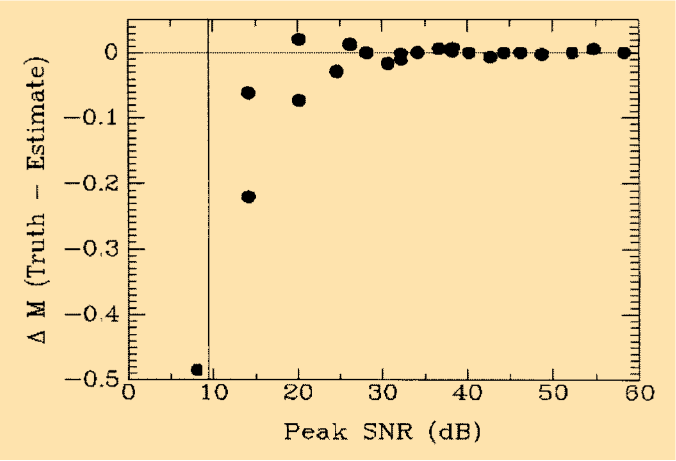

Figure 6: Residual photometry errors of Figure 5 plotted against the SNR of the 4 sources for the different SNR conditions. The horizontal dashed line represents perfect reconstruction and the vertical dashed line represents the 3σ noise level.

resolution of the algorithm permits it to be detected as a separate source.

Using multiple point-source objects makes it relatively easy to determine the reconstructed object fidelity permitting direct measurements of not only the astrometry, i.e. the relative positions of the sources, but also the relative photometry, i.e. the brightness of the sources. In all cases, the relative locations of the sources matches the truth. The relative photometry was computed, in stellar magnitudes, by measuring the peak pixel values of the four sources since the sources were all initially located at integer pixel locations. Figure 5 shows the residuals of the photometry as a function of the sources' true brightness values. Note that as the SNR decreases, the fidelity on the fainter source becomes worse in a systematic way with the magnitude difference increasing as the noise.

The reason for the underestimation of the fainter sources is because of the presence of the noise. This is further illustrated in Figure 6. This plots the residuals from Figure 5 against the SNR of each of the four sources for the six different SNR con-

*Figure 7: Reconstructed PSFs for (left to right) decreasing SNR for the first frame of the data cube. **Top:** the brightest source used as the initial PSF estimate. Note its contamination by the faintest source. **Bottom:** reconstructed PSFs.* ▼

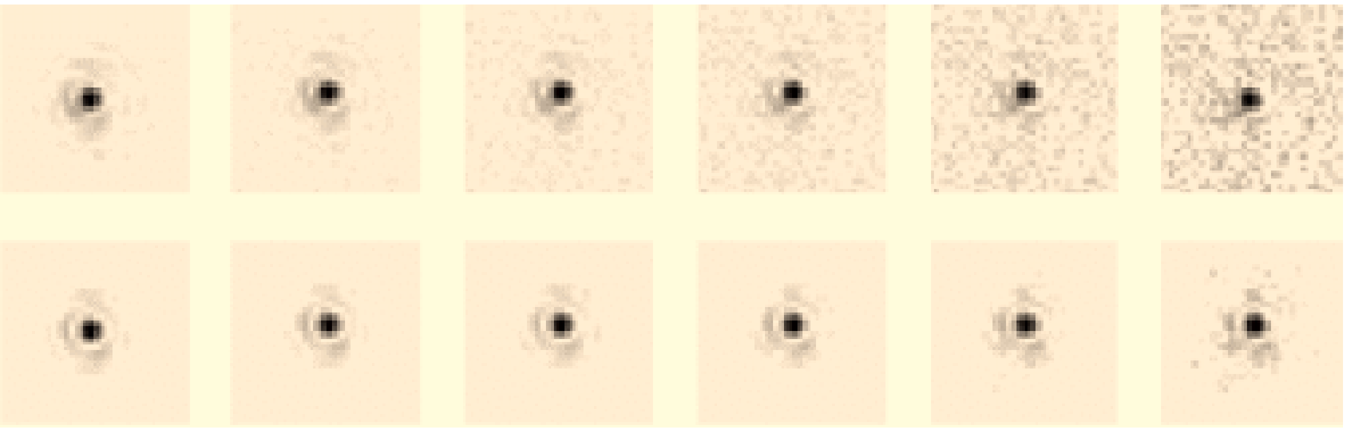

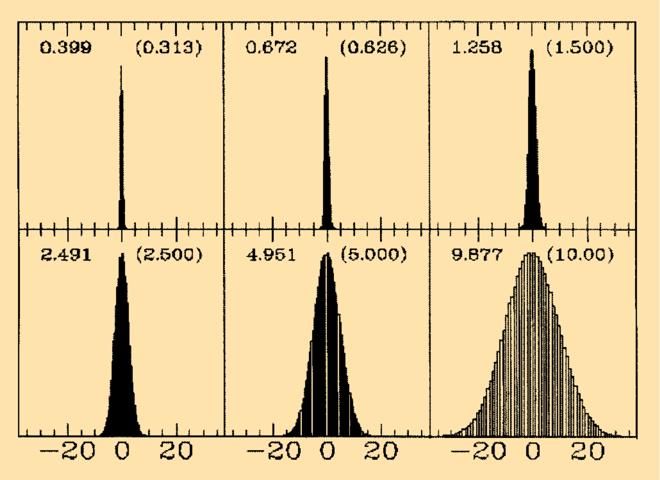

Figure 8: Histograms of the residuals for the six different SNR cases. The measured residuals rms value is shown for each case compared to the rms value of the input additive noise (in parentheses).

ditions. Note that the poorest reconstruction is below the 3σ level and that good reconstructions are obtained for SNRs greater than 6σ. This demonstrates that the sources that become "lost" in the noise are difficult to extract accurately.

As mentioned above, the object and the PSF are both reconstructed using deconvolution. Figure 7 shows the reconstructed PSF for the first data frame of the data cube for each of the SNR cases compared to the initial estimates for the first frame of the data cube. Comparison of the highest SNR case shows good agreement between the reconstruction and the "truth". As the SNR decreases, there is little difference in the reconstructions with more noise for the lowest SNR case. This analysis is useful when planning the observation's integration times, according to the desired photometric accuracy.

3.1.1 Effect of noise propagation

We ask "How well does the algorithm deal with the noise?" As seen above, some noise does appear in the object reconstructions and the PSFs, especially for the higher noise cases, but most of it shows up in the residuals. This is illustrated in Figure 8 which shows histograms of the residuals for the 6 different SNR reconstructions. As can be seen, these histograms appear to have Gaussian distributions. The rms value of the residuals compare very favourably to the input noise statistics and the residuals do have a zero-mean. The reduced photometric accuracy for the lower SNR cases shows the effect of the presence of noise on the algorithm's ability to break the symmetry between the PSF and the object, especially when using initial noisy PSF and object estimates.

These results demonstrate the algorithm's ability to recover not only the object distribution but also the corresponding PSFs for different SNR conditions. The residuals compare well to the input noise conditions, and relative photometry of the reconstructed object shows results consistent with the different SNRs. In all cases, 64 frames were reduced. For these data, the PSFs have a common diffraction-limited core but have different speckle noise. Thus, the multiple frames are significantly different from each other.

3.1.2 Effect of frame multiplicity

The next question we ask is "How well does the algorithm perform as the number of frames is reduced?" This was investigated by taking the third highest SNR data and reducing it using 1 set of 64 frames, 2 sets of 32 frames, 4 sets of 16 frames, 8 sets of 8 frames and 16 sets of 4 frames. The reconstructed object for the first of each of these sets is shown in Figure 9. Note that there appears to be little difference between them. The relative photometry of the four sources was calculated from the peak pixel values as above for all reconstructions. The mean and standard deviations were computed for the multiple reduction cases, i.e. when the number of frames was less than 64, and these are shown plotted in Figure 10. This shows the repeatability of the photometry and indicates that when the number of frames used is relatively small, i.e. ~ 8 or less, then the photometry on the fainter sources can show significant variation. There is also a trend that as the frame number decreases, the photometry of the fainter sources is underestimated. This is probably indicative of the combination of high noise and small number of frames making it difficult for the algorithm to distinguish between signal and noise.

3.2 Galaxy case

The multiple star represents imaging of a relatively simple object. A more typical extended target is that of a galaxy. Two sets of AO observations of a barely resolved galaxy were generated. The first using simulated AO PSFs for good compensation with SRs of ~ 50% which is typical of that expected by using e.g. a 60-element curvature system in *K*-band. The second had a much poorer compensation with SRs ~ 10% typical of a faint GS. The former data set were computed from simulated PSFs, whereas the latter was obtained from ADONIS observations of a faint isolated star. Each PSF data set comprised ten separate frames. These PSFs were over Nyquist sampled by a factor of two corresponding to an image scale of 32 mas/pixel assuming *K*-band imaging on a 3.6-m telescope.

The galaxy reference image for the simulations was obtained from the 512 × 512 galaxy image contained in the IRAF system. This was reduced using 8 × 8 pixel block sums to a 64 × 64 pixel image which was then embedded in a 128 × 128 pixel field. This image was then convolved with the PSFs and then contaminated by zero-mean additive noise with PSNRs of 1000, 200 and 50 corresponding to dynamic ranges of 7.5, 5.8 and 4.2 magni-

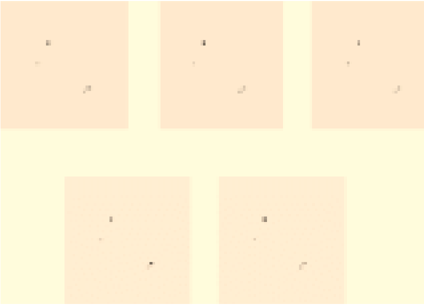

Figure 9: Reconstructed object for the third highest SNR case for (left to right and top to bottom) 4, 8, 16, 32, and 64 frame reductions.

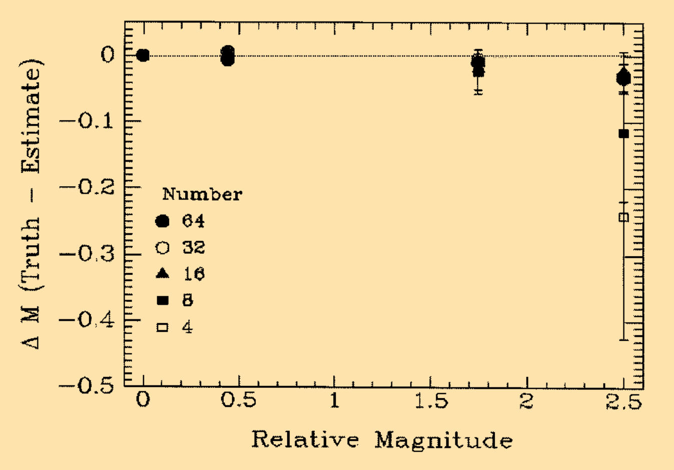

Figure 10: Residual photometry errors from measuring the brightest pixel for each of the four sources in the object reconstructions for the different multiple-frame reductions. The mean and standard deviations are shown for the reductions using less than 64 frames.

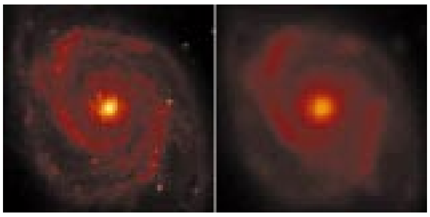

Figure 11: Simulated AO galaxy observations for high SR (left) and low SR (right). (Displayed on a square-root scale intensity.)

tudes respectively. Figure 11 shows the uncontaminated mean observation for the two SNR cases obtained from shift-and-add analysis.

Figure 12 illustrates the effect of the additive noise on the resolution of the images. The complete average power spectrum of the ten frames for the 3 SNR cases of the lower SR data radial profiles are shown. Also shown are the noise bias levels. Where they intersect with the data spectrum is more clearly seen in the top panel which shows the SNR of the measured power spectrum. Note that the highest spatial-frequency passed by the pupil is set to unity and for a PSNR of 1000, this is reached. However, as the noise increases, the effective frequency cut-off decreases to 0.85 for a PSNR of 200 and to 0.52 for a PSNR of 50. Thus, high spatial frequency information is further corrupted by the additive noise.

The data sets were reduced using the noisy SAA image as the initial object estimate and a SAA of a reference star as the initial PSF. This PSF estimate was obtained from the same set of data, which created the galaxy images, but excluding the used PSFs. The iterations were terminated when the noise bias level was reached. Full-field support was used for the object and the PSFs as well as the band-limit. All six cases have been analysed (3 SNRs each for the two SR cases). For both SR cases, it can be seen in the curves of Figure 13 that as the SNR decreases, the effective resolution also decreases. Also, the higher the initial SR, the better the reconstruction. Super-resolution is achieved over the diffraction-limited image for all but the lowest SNR case for the lower Strehl data, which is restored to diffraction-limited. The reconstructions show the detectability of the spiral arm structure lost in the raw compensated images.

Figure 13 shows the radial profiles of the Fourier moduli of the low SR reconstructed images compared to the truth (the top line of the four). The vertical lines indicate the noise-effective cut-off frequency f_N (see Fig. 12) for the three SNRs. These plots show that within f_N, there is good reconstruction but for the super-resolution regime, in these cases for $f > f_N$, the higher spatial frequencies are attenuated with respect to the truth. In order to quantitatively measure how good the reconstruction is, the normalised cross-spectrum was computed between the reconstruction and the truth, i.e.

$$XS_i = \frac{|F_i \cdot \hat{F}_i^*|}{F_i \cdot F_i^*} \qquad (12)$$

which will be unity for a perfect correlation. Note that the numerator is the modulus of the cross-spectrum only so that mis-registration of the two images does not affect the value. The summation of XS_i, yields the correlation coefficient for the reconstruction, i.e.

$$\gamma_\Lambda = \sum_{i \in \Lambda} XS_i \qquad (13)$$

where Λ represents the spatial frequency region over which the summation is computed. Setting Λ to the SNR support (see Figure 12) yields correlation coefficients of 1.1, 1.0 and 0.9 for decreasing signal-to-noise showing excellent reconstruction within those regimes.

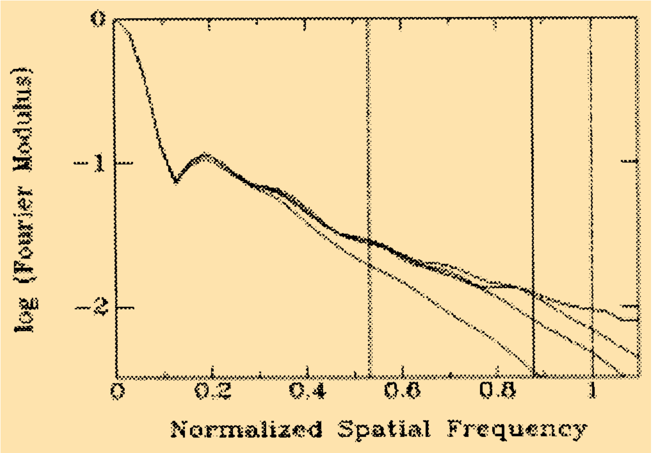

Figure 13: Azimuthally averaged radial profiles of the Fourier moduli of the reconstructed images for the lower SR data. Decreasing SNR gives lower spatial frequency cutoff and worse MTF.

4. Application to ADONIS Data

In this section, we present results of the IDAC algorithm as applied to different types of measured data. This includes binary stars, then the Galilean satellite Io as an extended object, and R Aqr, which has faint structure around a bright central source.

4.1. Closeby point sources: τ Canis Majoris

Data were taken of the bright binary star τ CMa (= HR2782 = ADS 5977A) at the ESO 3.6-m during a technical run in February 1996. The Yale Bright Star Catalogue lists it as being an O91b star of m_v = 4.40, having an equal magnitude companion at a separation of 0.2″. More recently, the CHARA group have measured it obtaining a separation of 0.160″ in 1989.9 (Hartkopf et al., 1993). The diffraction-limits of the telescope are 0.072″ at J (1.25μm), 0.095″ at H (1.65μm) and 0.126″ at K (2.2μm). Thus the data were Nyquist-sampled at J, i.e. at 0.035″/pix-

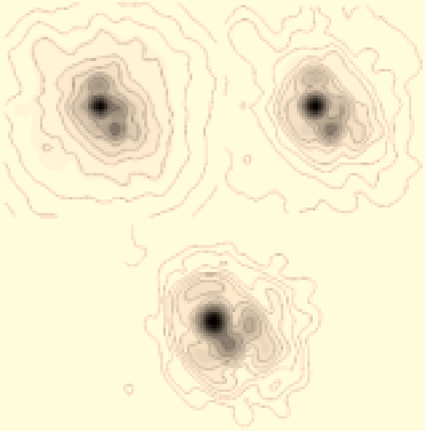

Figure 14: J (top left), H (top right), and K-band (bottom) peak tracked images (smoothed to remove the pixel-to-pixel variations) with superimposed logarithmic contours emphasising the extended halo structure in the images. The contour levels are at 1, 1.6, 2.5, 4, 6.3, 10, 16, 25, 40, 63% of the peak value in each of the images.

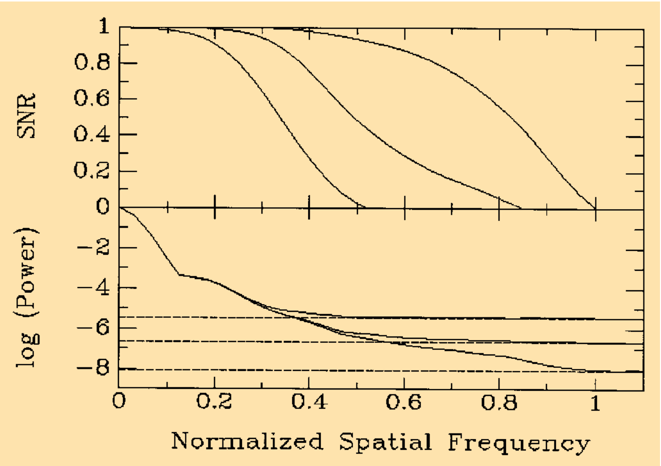

Figure 12: How noise affects resolution. The bottom panel shows azimuthally averaged power spectra for the three SNR observations of the lower SR data. The top panel shows the corresponding SNR. Note that as the noise increases the cut-off frequency decreases.

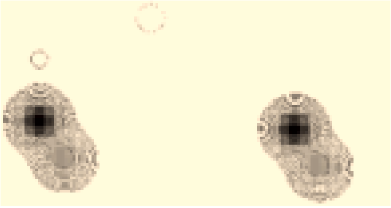

Figure 15: J-band τ CMa object reconstructions for the first (left) and second (right) 16 frames. Same contour levels as Figure 14.

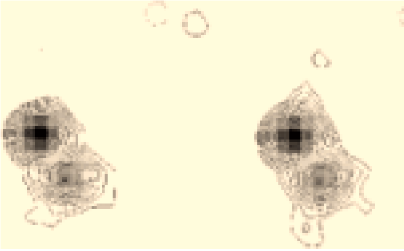

Figure 16: H-band τ CMa object reconstructions for the first (left) and second (right) 16 frames. Same contour levels as Figure 14.

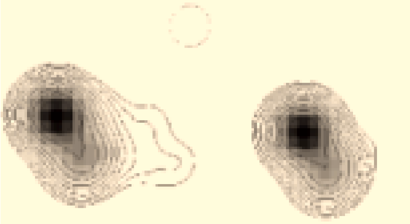

Figure 17: K-band τ CMa object reconstructions for the first (left) and second (right) 16 frames. Same contour levels as Figure 14.

el and over-sampled at the longer wavelengths easily resolving the companion. The data were taken in "speckle" mode, i.e. using a series of 200 short exposures (t_{exp} = 50 ms) with a sample time of Δt = 0.74s. Seeing was estimated to be 0.8″ at visible wavelengths (0.55μm). The AO loop was operated at maximum gain with the Shack-Hartman Reticon sensor in line mode, at a rate of 200Hz.

The initial data post-processing consisted of background correction and flat fielding with bad-pixel correction. Figure 14 shows SAA images for the three observing bands. These clearly show the companion but they are also contaminated by extended halo due to the residual wavefront errors of the AO compensation as well as a "fixed-pattern" error in the form of triangular coma giving rise to a "lumpy" Airy ring about the image cores. These clearly illustrate the need for deconvolution.

In the initial application of the algorithm, the original 200-frame data sets were reduced to sub-sets of 16 frames of 64 × 64 pixels i.e. 2.24″ × 2.24″. Thus, there were $(M+1)N^2$ = 69632 variables to be minimized for M convolution images of size $N \times N$. For all three wavebands, the first 16 frames were used and the initial object estimates were the SAA images shown in Figure 14. As no prior PSF knowledge existed, the *initial* PSF estimates were chosen to be Gaussians. The super-resolved images were filtered back with a Gaussian of FWHM = 0.083″ which slightly over resolves the diffraction-limit at this wavelength, i.e. λ/D ≈ 0.12″. Figures 15, 16 and 17 show the reconstructed objects for the three wavebands obtained from the first and second sets of 16 frames of the 200-frame data sets. Note the strong similarity between the image pairs with differences occurring only at the few-percent level and also note how clean the reconstructions are.

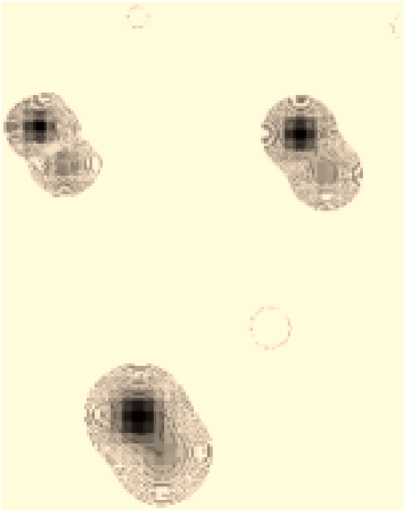

Figure 18: Final Gaussian smoothed J (top left), H (top right) and K-band (bottom) τ CMa object reconstructions using all 200 data frames and an SH start. Same contour levels as Figure 17.

Keith Hege at Steward Observatory has suggested that Speckle Holography (SH) (Hege, 1989) imposes a further constraint on the data. This is applied outside of the blind deconvolution loop and may prevent stagnation into a local minimum. It makes use of a multiple-frame data set along with PSF estimates for each frame. The object estimate was obtained as follows, i.e.

$$\hat{f}_i = \mathrm{FT}^{-1}\left[\hat{F}_u\right] = \mathrm{FT}^{-1}\left[\frac{\langle G_u \cdot \hat{H}^*_u \rangle}{\langle H_i \cdot \hat{H}^*_i \rangle}\right]$$

$$= \mathrm{FT}^{-1}\left[F_u \frac{\langle H_u \cdot \hat{H}^*_u \rangle}{\langle \hat{H}_u \cdot \hat{H}^*_u \rangle}\right] \qquad (14)$$

so that when the PSF estimates equal the true PSFs then the band-limited object estimate will equal the true band-limited object. This multiple-frame deconvolution has been shown to be less noise sensitive than deconvolving on a frame-by-frame basis. The object estimate from this procedure coupled with the PSFs, which produced it, can then be fed back into the myopic deconvolution code as new estimates.

Band	Δr (mas)	PA (°)	Δ*m*
J	149	34	0.84
H	149	33	0.80
K	149	33	0.94

Table 2: Astrometry and photometry for the 200-frame τ CMa blind deconvolutions reconstructions for the three wavebands.

For the three data sets reported here, a variant of this was performed. The PSFs for all 200 frames at each waveband were computed by simply taking the super-resolved object estimate (from the first 16-frame start-up sub-set, using Gaussian PSFs) and deconvolving into each measured data frame. These were then used as the PSF estimates in equation (2) to generate a new object estimate. Blind deconvolution was then applied to all 200 frames for each waveband. The resulting object estimates are shown in Figure 18.

These images show a very clean deconvolution with lack of background features below the 1% levels. The astrometry and photometry of the final images obtained by Gaussian fits are given in Table 2 and show very self-consistent astrometry for the three wavebands.

4.2. Io observations

The Jovian Galilean satellite, Io, is typical of the type of Solar-System objects which are benefitted by AO observations. At thermal infrared wavelengths, the volcanic hot spots can be detected against the cooler background surface without waiting for the moon to go into eclipse. Its volcanic activity is monitored from the ground using the thermal camera facility (COMIC) which is available on the ADONIS system at the ESO 3.6-m (Le Mignant et al. 1998). It was observed in September 1998 in the L' band (λ = 3.809, Δλ = 0.623 μm) with an image scale of 0.100″/pixel, corresponding to ≈ 400 km on the surface of Io, and an integration time of 500 msec. The source had a visual magnitude of m_{v} = 5.1, and measurements of the seeing using the Differential Image Motion

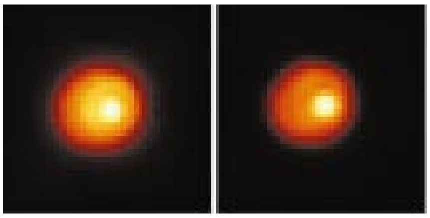

Figure 19: ADONIS imaging of Io. The ensemble average of a set of ten exposures is shown on the left and the reconstructed object is shown on the right.

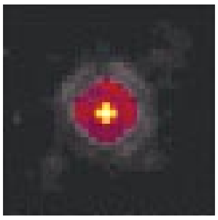

Figure 20: Ensemble average reference star (PSF calibrator) image for the Io observations.

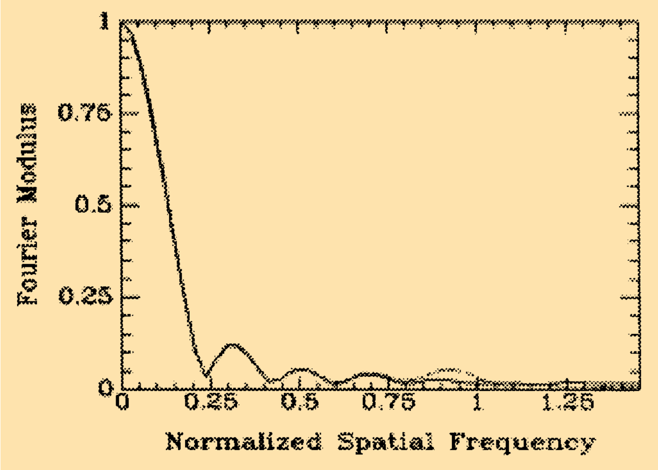

Figure 22: Azimuthally averaged radial profiles through the Fourier modulus of the pixel-limited truth image (solid-line, see Figure 24) and the reconstructed image (dashed line).

Monitor (DIMM) was 0.75″. At this wavelength the 3.6-m has a diffraction-limit of 0.226″ so that the object was well oversampled. A PSF calibrator with similar visible brightness HD174974 (m_v = 5.0, G5) was observed to yield initial PSF estimates. The field of view of the observations was 12.8″ × 12.8″.

The data set comprised ten separate observations of Io, the complete average is shown in Figure 19. This was used as the initial object estimate. The mean of the point source calibrator was used as the initial PSF estimate, shown in Figure 20. Note that the PSF is diffraction-limited with a Strehl ratio of ~ 50%.

The reconstructed object is also shown in Figure 19. This has been regularised by suppressing the high-spatial frequency information with apodisation by a perfect telescope transfer function. Thus, the effective resolution is the same as for the observation, but now the “hot spot” on the satellite’s surface, Loki, is more clearly discerned against the smooth distribution of the surface.

The algorithm’s ability to super-resolve has been discussed earlier. For objects with sharp edges, such as a planetary satellite or asteroid, truncation of the high spatial frequencies results in “ringing” in the image domain. The super-resolution achieved on these types of objects has been discussed previously (Christou et al., 1994) and is further illustrated below with simulations of Io imaging. Figure 21 compares a simulated Io object, i.e. a uniform disk with two hot-spots, to the reconstruction, both of them for super-resolution which is ~ 1.5 × diffraction-limited case. As can be seen, these two images (top-right and bottom-right) agree very well. Just how well, is better seen in the Fourier moduli of the truth image compared to the reconstruction before filtering. This is shown with the azimuthally averaged radial profiles in Figure 22.

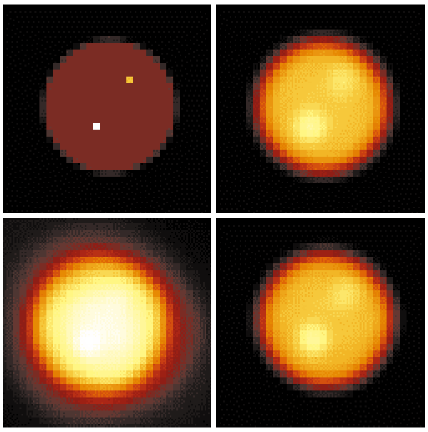

Figure 21: Simulated observations and reductions of an Io-type object: truth (top left), filtered truth (top right), observation (bottom left) and filtered reduction (bottom-right).

The radial profiles match well out to ~ 80% of the diffraction-limit where the reconstruction has greater power than the truth. Beyond the diffraction-limit, the reconstruction has non-zero power but at a lower level than the truth. The spatial frequency range shown indicates the region over which the filtered images in Figure 21 were restored.

A thorough analysis of Io adaptive optics imaging and the resulting science can be found in a recent article by Marchis et al. (1999).

4.3 R Aquarii

R Aquarii is an eclipsing symbiotic binary surrounded by morphologically complex nebulosity which extends to ~ 1 arcminute from the central source. At smaller scales, there is an elongated jet-like emission feature (Hollis et al., 1985). It was observed in December 1996 with ADONIS equipped with a Fabry-Perot at the ESO 3.6-m in both the 2μm continuum and the Hydrogen emission line, Brγ (2.1655μm) in order to detect and resolve structures of the nebulosity. The image scale was 0.05″/pixel with exposure times of 0.6s for a total integration time of 48s, for the Brγ observations reduced here. The individual frame PSNR was computed to be ~ 2000 for the central source but for the nebulosity, ~ 3″ away, it was ~ 5. In order to improve the SNR, the data were binned down from 80 to 10 frames, increasing the nebulosity SNR to ~ 15.

The 10 eight-frame-binned data were reduced using the PSF constraint (see equation 8) in addition to the band-limit and fidelity terms, where the “known” PSF was obtained from the shift-and-add image of the central source for all 80 observations. After convergence, the processing was continued with the PSF constraint removed. Figure 23 compares the nebulosity and central source for a single observation, an eight-frame average, as used for the deconvolution showing the improved SNR, and for the 80-frame sum. The reconstructed objects are shown in Figure 24 for both the Brγ and continuum observations, both with and without the PSF constraint. The initial estimate in each case was the Richardson-Lucy reconstruction. Note how after the PSF constraint is “relaxed”, the morphology of the nebulosity changes to better fit the observations. This nebulosity has structure on the scale of ~ 0.1″, i.e. diffraction-limited and there are obvious structural differences between the two wavebands.

5. Discussion

In this article we have shown the effectiveness of using a multi-frame iterative myopic deconvolution technique on AO data. Using the IDAC SW on both simulations and real data, it is shown that it is a powerful tool for deconvolving AO images, to remove the effects of the uncompensated components of the PSFs

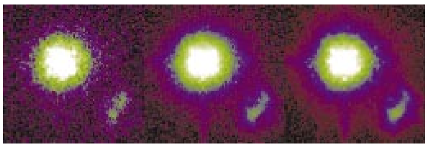

Figure 23: R Aquarii observations in Brγ. Single frame (left), 8-frame average (centre) and 80-rame average (right).

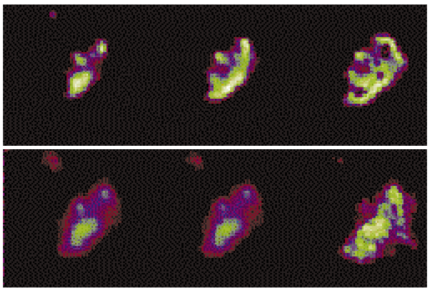

Figure 24: R Aquarii nebulosity reductions: Brγ (top) and 2 μm continuum (bottom). Left to right are the Richardson-Lucy reductions used for the initial object estimate, the PSF constrained IDAC reduction and the PSF relaxed reconstruction.

and reach full diffraction performances. The ESO ADONIS PSFs show a variability, which is common to AO systems. It is this variability and the lack of a precise frame-by-frame PSF determination that makes post-processing of the data difficult. The iterative multiframe deconvolution method described takes successfully advantage of this intrinsic variability.

The linearity of the algorithm and its preservation of photometry is demonstrated on the four star simulations.

Multi-frame iterative myopic deconvolution enforces the very important constraint that observations of the same object will yield a common object result. Some prior PSF information is extremely useful in reducing the search space for the solution as demonstrated by the R Aquarii results.

Observations of a PSF calibrator, as demonstrated here, make an excellent initial PSF estimate, and this can be further strengthened by application of the PSF constraint. A variation on this approach has been utilised by Conan et al. (1997) and Véran et al. (1997). They have demonstrated that a very good initial PSF estimate can be obtained from a statistical analysis of the residual wavefront errors. Currently, this approach is applicable only to AO systems using photon counters, but it should be extendable to wavefront sensor systems using detectors with read-out noise as well, such as CCDs. Combined statistical PSF estimation and blind deconvolution post-processing has been discussed by Fusco et al. (1998) and Christou et al. (1997).

6. Acknowledgements

We would like to thank the ESO staff at La Silla 3.6-m for the effective observing support during the observing runs. We would also like to thank Keith Hege, Matt Chesalka and Stuart Jefferies for the IDAC code and for useful discussions about its application. This work was supported by the Adaptive Optics Group of the Instrumentation Division, at the European Southern Observatory.

Bibliography

Christou, J.C., Hege, E.K., Jefferies, S.M., & Keller, Ch.U., 1994, *Proc SPIE*, ed. J.B. Breckenridge, **2200**, 433–444.

Christou, J.C., Bonaccini, D., & Ageorge, N., 1997, *Proc. SPIE*, ed. R.K. Tyson & R.Q. Fugate, **3126**, 68–80.

Christou, J.C., Marchis, F., Ageorges, N., Bonaccini, D., & Rigaut, F. 1998a, ed. D. Bonaccini & R.Q. Fugate, **3353**, 984–993.

Christou, J.C., Hege, E.K., Jefferies, S.M., & Cheselka, M., 1998b, *Proc. SPIE*, ed. A.D. Devir, A. Kohnle, U. Schreiber, & C. Werner, **3494**, 175–186.

Le Mignant, D., Marchis, F., Bonaccini, D., et al., 1998, *Proc ESO/OSA*, ed. D. Bonaccini, **56**, 287–301.

Marchis, F., Prangé, R., Christou, J.C., 1999, *Icarus*, submitted.

Fusco, T., Véran, J.-P., Conan, J.-M., & Mugnier, L.M., 1999, *Astron. Astrophys.*, **134**, 193.

Hartkopf, W.I., Mason, B.D., Barry, D.J., McAlister, H.A., Bagnuolo, W.G., & Prieto, C.M., 1993, *Astron. J.*, **106**, 352.

Hollis, J.M., Kafatos, M., Michalitsianos, A.G., & McAlister, H.A., 185, *Astrophys. J.*, **289**, 765.

Jefferies, S.M. & Christou, J.C., *Astrophys. J.*, 1993, **415**, 862.

Lucy, L., 1974, *Astrophys. J.*, **79**, 745.

Sheppard, D.G., Hunt, B.R., & Marcellin, M.W., 1998, *J. Opt. Soc. Am. A.*, **15**, 978–992.

Thiébaut, E., & Conan., J.-M., *J. Opt. Soc. Am. A.*, 1994, **12**, 485.

Véran, J.P., Rigaut, F., Maître, H., & Rouan, D., 1997, *J. Opt. Soc. Am. A.*, **14**, 3057.

LATEST NEWS

“First Light” for VLT High-Resolution Spectrograph UVES

(Excerpt from ESO Press Release 15/99, 5th October 1999)

A major new astronomical instrument for the ESO Very Large Telescope at Paranal (Chile), the UVES high-resolution spectrograph, made its first observations of astronomical objects on September 27, 1999. The astronomers are delighted with the quality of the spectra obtained at this moment of “First Light”. Although much fine-tuning still has to be done, this early success promises well for new and exciting science projects with this large European research facility.

Astronomical Instruments at VLT KUEYEN

The second VLT 8.2-m Unit Telescope, KUEYEN (“The Moon” in the Mapuche language), is in the process of being tuned to perfection before it will be “handed” over to the astronomers on April 1, 2000.

The testing of the new giant telescope has been successfully completed. The latest pointing tests were very positive and, from real performance measurements covering the entire operating range of the telescope, the overall accuracy on the sky was found to be 0.85 arcsec (the RMS-value). This is an excellent result for any telescope and implies that KUEYEN (as is already the case for ANTU) will be able to acquire its future target objects securely and efficiently, thus saving precious observing time.

The three instruments foreseen at KUEYEN are UVES, FORS2 and FLAMES. They are all dedicated to the investigation of the spectroscopic properties of faint stars and galaxies in the Universe.

The UVES Instrument

The Ultraviolet Visual Echelle Spectrograph (UVES) is the first instrument on Kueyen. It was built by ESO, with the collaboration of the Trieste Observatory (Italy) for the control software. Complete tests of its optical and mechanical components, as well as of its CCD detectors and of the complex control system, were made in the laboratories of the ESO Headquarters in Garching (Germany) before it was fully dismounted and shipped to the ESO Paranal Observatory, 130 km south of Antofagasta (Chile). There, the different pieces of UVES (with a total weight of 8 tons) were carefully reassembled on the Nasmyth platform of KUEYEN and made ready for real observations.

UVES is a complex two-channel spectrograph that has been built around two giant optical (echelle diffraction) gratings, each ruled on a 84 cm × 21 cm × 12 cm block of the ceramic material Zerodur (the same that is used for the VLT 8.2-m main mirrors) and weighing more than 60 kg. These echelle gratings disperse the light from celestial objects collected by the telescope into its constituent wavelengths (colours).

UVES’ resolving power (an optical term that indicates the ratio between a given wavelength and the smallest wavelength difference between two spectral lines that are clearly separated by the spectrograph) may reach 110,000, a very high value for an astronomical instrument of such a large size. This means for instance that even comparatively small changes in radial ve-